

# Crossover between Kelvin-Helmholtz and counter-superflow instabilities in two-component Bose-Einstein condensates

Naoya Suzuki,<sup>1</sup> Hiromitsu Takeuchi,<sup>2</sup> Kenichi Kasamatsu,<sup>3</sup> Makoto Tsubota,<sup>2</sup> and Hiroki Saito<sup>1</sup>

<sup>1</sup>*Department of Engineering Science, University of Electro-Communications, Tokyo 182-8585, Japan*

<sup>2</sup>*Department of Physics, Osaka City University, Sumiyoshi-ku, Osaka 558-8585, Japan*

<sup>3</sup>*Department of Physics, Kinki University, Higashi-Osaka, Osaka 577-8502, Japan*

(Dated: September 10, 2010)

Dynamical instabilities at the interface between two Bose-Einstein condensates that are moving relative to each other are investigated using mean-field and Bogoliubov analyses. Kelvin-Helmholtz instability is dominant when the interface thickness is much smaller than the wavelength of the unstable interface mode, whereas the counter-superflow instability becomes dominant in the opposite case. These instabilities emerge not only in an immiscible system but also in a miscible system where an interface is produced by external potential. Dynamics caused by these instabilities are numerically demonstrated in rotating trapped condensates.

## I. INTRODUCTION

When wind blows over a water surface, the relative motion between the water and the air generates instabilities at the interface; these instabilities in turn produce waves. Such interfacial instabilities between two fluids that are moving relative to each other are referred to as Kelvin-Helmholtz instabilities (KHIs) [1–3] and they are found throughout nature. A system of superfluids is an ideal testing ground for KHIs because of the absence of viscosity. The Helsinki group experimentally realized shear flow between the A and B phases of superfluid <sup>3</sup>He in a rotating cryostat. They observed vortices penetrating from the A phase into the B phase due to KHIs [4, 5].

Recently, KHIs and nonlinear dynamics of quantized vortices have been investigated for a gaseous two-component Bose-Einstein condensate (BEC) with relative velocity [6]. In Ref. [6], it is assumed that the two components are strongly segregated and that the interface thickness is much smaller than the wavelengths of unstable interface modes. If, however, the two components are weakly segregated, they strongly overlap with each other at the interface, at which the two components coexist with a relative velocity. Law *et al.* [7] showed that two miscible BECs moving through each other exhibit a dynamical instability, which we refer to as a counter-superflow instability (CSI). The dynamics generated by CSIs have recently been experimentally observed [8]. We therefore expect that KHIs compete with CSIs as the thickness of the interface is increased and that CSIs become important in the weakly segregated regime.

In the present paper, we investigate both KHI and CSI on an equal footing in a phase-separated two-component BEC with relative velocity. We show that KHIs and CSIs are respectively generated for thin and thick interfaces; the interface thickness is controlled by the repulsive interaction between the two components and external forces. The numerically obtained stability boundaries in the parameter space are well described by the KHI in the thin interface limit and by the CSI in the uniform overlap limit. We propose various experimental situations for

observing these instabilities in trapped systems.

This paper is organized as follows. Section II reviews KHIs and CSIs in BECs, and performs the mean-field and Bogoliubov analyses for a system with a flat interface. Sections III and IV propose experimental systems for generating these instabilities in pancake-shaped and cigar-shaped traps, respectively, and numerically demonstrate the nonlinear dynamics caused by these instabilities. Section V presents the conclusions of this study.

## II. INSTABILITIES AT AN IDEAL INTERFACE

### A. Kelvin-Helmholtz instability

We first formulate a KHI in a strongly segregated two-component BEC with relative velocity between its two components [9]. In the mean-field theory, the two-component BEC is described by the macroscopic wave functions  $\psi_1$  and  $\psi_2$ . The Lagrangian for the system is given by

$$L = \int d\mathbf{r} (P_1 + P_2 - g_{12}|\psi_1|^2|\psi_2|^2), \quad (1)$$

where

$$P_j = i\hbar\psi_j^* \frac{\partial \psi_j}{\partial t} + \frac{\hbar^2}{2m_j} \psi_j^* \nabla^2 \psi_j - U_j |\psi_j|^2 - \frac{g_{jj}}{2} |\psi_j|^4 \quad (2)$$

with  $m_j$  and  $U_j$  being the atomic mass and the external potential of the  $j$ th component, respectively. The inter- and intra-component interaction parameters have the form,

$$g_{jj'} = 2\pi\hbar^2 a_{jj'} (m_j^{-1} + m_{j'}^{-1}), \quad (3)$$

where  $a_{jj'}$  is the s-wave scattering length between the  $j$ th and  $j'$ th components. The interaction parameters are assumed to satisfy the phase-separation condition [10],

$$g_{11}g_{22} < g_{12}^2. \quad (4)$$

We assume that components 1 and 2 are respectively located in  $y \lesssim 0$  and  $y \gtrsim 0$  and that the interface between the two components is located near the  $y = 0$  plane. In this subsection, we neglect the interface thickness and introduce an interface tension coefficient  $\alpha$  [11–13], which originates from the excess energy at the interface. The Lagrangian can thus be rewritten as

$$L = \int dx dz \left( \int_{-\infty}^{\eta} dy P_1 + \int_{\eta}^{\infty} dy P_2 \right) - \alpha S, \quad (5)$$

where  $y = \eta(x, z, t)$  is the position of the interface and

$$\begin{aligned} S &= \int dx dz \left[ 1 + \left( \frac{\partial \eta}{\partial x} \right)^2 + \left( \frac{\partial \eta}{\partial z} \right)^2 \right]^{1/2} \\ &\simeq \int dx dz \left[ 1 + \frac{1}{2} \left( \frac{\partial \eta}{\partial x} \right)^2 + \frac{1}{2} \left( \frac{\partial \eta}{\partial z} \right)^2 \right] \end{aligned} \quad (6)$$

is the area of the interface. Taking the functional derivative of the action  $\int dt L$  with respect to  $\eta(x, z, t)$  and setting it to zero, we obtain

$$P_1(y = \eta) - P_2(y = \eta) + \alpha \left( \frac{\partial^2 \eta}{\partial x^2} + \frac{\partial^2 \eta}{\partial z^2} \right) = 0, \quad (7)$$

which corresponds to the Bernoulli equation in hydrodynamics.

We consider a stationary state in which the  $j$ th component flows in the  $x$  direction with a velocity  $V_j$  as

$$\Psi_j = \sqrt{n_j(y)} \exp \left[ \frac{i}{\hbar} (-\mu_j t + m_j V_j x) \right], \quad (8)$$

where  $\mu_j$  is the chemical potential for the  $j$ th component. The potential  $U_j(y)$  and the density distribution  $n_j(y)$  are assumed to depend only on  $y$ , where  $n_1 = 0$  for  $y > \eta$  and  $n_2 = 0$  for  $y < \eta$  are satisfied. Substituting Eq. (8) into Eq. (7) with  $\eta = 0$  gives the equilibrium condition for the pressure,  $g_{11}n_1^2/2 = g_{22}n_2^2/2$ .

We assume that the system is approximately incompressible. A small deviation from the stationary state in this case is described as

$$\psi_j = \Psi_j \exp \left[ i A_j e^{-(1)^j k y} \cos(kx - \omega t) \right], \quad (9)$$

$$\eta = a \sin(kx - \omega t), \quad (10)$$

where  $A_j$  and  $a$  are infinitesimal parameters. From the kinematic boundary condition, the interface velocity in the  $y$  direction  $(\partial/\partial t + V_j \partial/\partial x)\eta$  must be equal to  $\hbar/(im_j n_j) \psi_j^* \partial \psi_j / \partial y|_{y=\eta}$ , giving

$$-(-1)^j \frac{\hbar}{m_j} A_j k e^{-(1)^j k \eta} = (V_j k - \omega) a. \quad (11)$$

Substituting Eqs. (9)-(11) into Eq. (7) and neglecting second and higher orders of  $A_j$  and  $a$ , we obtain

$$\frac{\rho_1}{k} (\omega - V_1 k)^2 - f_1 n_{s1} = -\frac{\rho_2}{k} (\omega - V_2 k)^2 - f_2 n_{s2} + \alpha k^2, \quad (12)$$

where  $n_{s1} = n_1(\eta + 0_-)$ ,  $n_{s2} = n_2(\eta + 0_+)$ ,  $\rho_j = m_j n_{sj}$ , and  $f_j = U'_j(\eta)$ . Equation (12) gives the dispersion relation,

$$\omega = \frac{(\rho_1 V_1 + \rho_2 V_2)k}{\rho_1 + \rho_2} \pm \sqrt{-\frac{\rho_1 \rho_2 (V_1 - V_2)^2 k^2}{(\rho_1 + \rho_2)^2} + \frac{Fk + \alpha k^3}{\rho_1 + \rho_2}}, \quad (13)$$

where  $F = n_{s1} f_1 - n_{s2} f_2$ .

We note that Eq. (13) has the same form as the dispersion relation for the KHI in classical incompressible and inviscid fluids [3]. When  $F > 0$  and

$$(V_1 - V_2)^4 \geq 4\alpha F \frac{(\rho_1 + \rho_2)^2}{\rho_1^2 \rho_2^2} \equiv V_{cr}^4, \quad (14)$$

a dynamical instability arises for  $k_- < k < k_+$ , where

$$k_{\pm} = \frac{\rho_1 \rho_2 (V_1 - V_2)^2}{2\alpha(\rho_1 + \rho_2)} \left[ 1 \pm \sqrt{1 - \frac{V_{cr}^4}{(V_1 - V_2)^4}} \right]. \quad (15)$$

The most unstable wave number is given by

$$k = \frac{\rho_1 \rho_2 (V_1 - V_2)^2}{3\alpha(\rho_1 + \rho_2)} \left[ 1 + \sqrt{1 - \frac{3V_{cr}^4}{4(V_1 - V_2)^4}} \right]. \quad (16)$$

For  $|V_1 - V_2| < V_{cr}$ , the system is dynamically stable. When  $F = 0$ ,  $V_{cr}$  vanishes and the system is dynamically unstable for  $|V_1 - V_2| > 0$ . In this case, the range of unstable wave numbers is given by

$$0 < k < \frac{\rho_1 \rho_2 (V_1 - V_2)^2}{\alpha(\rho_1 + \rho_2)}. \quad (17)$$

From Eq. (13), we find that the group velocity  $d\omega/dk$  diverges for  $k \rightarrow 0$  and  $F > 0$ . This unphysical behavior originates from the incompressibility approximation in Eq. (9). For  $F < 0$ , the system is always dynamically unstable even when  $V_1 - V_2 = 0$ , which is referred to as a Rayleigh–Taylor instability [14–16].

## B. Counter-superflow instability

We review the derivation of the Bogoliubov spectrum for a system of a uniform two-component BEC with a relative velocity [7]. The functional derivative of  $\int dt L$ , where  $L$  is the Lagrangian in Eq. (1), with respect to  $\psi_j^*$  gives the Gross-Pitaevskii (GP) equation ( $j \neq j'$ ),

$$i\hbar \frac{\partial \psi_j}{\partial t} = -\frac{\hbar^2}{2m_j} \nabla^2 \psi_j + U_j \psi_j + g_{jj} |\psi_j|^2 \psi_j + g_{jj'} |\psi_{j'}|^2 \psi_j. \quad (18)$$

We assume  $U_j = 0$  and the miscible condition,

$$g_{11}g_{22} > g_{12}^2, \quad (19)$$

in this subsection. We consider a small excitation  $\phi_j$  above a uniform state with a velocity  $\mathbf{V}_j = \hbar \mathbf{K}_j / m_j$  as

$$\psi_j = (\sqrt{n_j} + \phi_j) e^{-i\mu_j t / \hbar + i\mathbf{K}_j \cdot \mathbf{r}}, \quad (20)$$

where  $\mu_j = g_{jj}n_j + g_{jj'}n_{j'} + \hbar^2 K_j^2/(2m_j)$ . Substituting Eq. (20) into Eq. (18) and taking the first order of  $\phi_j$ , we obtain ( $j \neq j'$ )

$$i\hbar \frac{\partial \phi_j}{\partial t} = \left[ -\frac{\hbar^2}{2m_j} (\nabla + i\mathbf{K}_j)^2 - \mu_j + 2g_{jj}n_j + g_{jj'}n_{j'} \right] \phi_j + g_{jj}n_j\phi_j^* + g_{jj'}\sqrt{n_j n_{j'}} (\phi_{j'} + \phi_{j'}^*). \quad (21)$$

We expand the small excitation as

$$\phi_j = u_{j\mathbf{k}} e^{i\mathbf{k}\cdot\mathbf{r} - i\omega t} - v_{j\mathbf{k}}^* e^{-i\mathbf{k}\cdot\mathbf{r} + i\omega t}, \quad (22)$$

and substitute it into Eq. (21), giving ( $j \neq j'$ )

$$\left[ \frac{\hbar^2}{2m_j} (k^2 + 2\mathbf{k} \cdot \mathbf{K}_j) + g_{jj}n_j \right] u_{j\mathbf{k}} - g_{jj}n_j v_{j\mathbf{k}} + g_{jj'}\sqrt{n_j n_{j'}} (u_{j'\mathbf{k}} - v_{j'\mathbf{k}}) = \hbar\omega u_{j\mathbf{k}}, \quad (23a)$$

$$\left[ \frac{\hbar^2}{2m_j} (k^2 - 2\mathbf{k} \cdot \mathbf{K}_j) + g_{jj}n_j \right] v_{j\mathbf{k}} - g_{jj}n_j u_{j\mathbf{k}} - g_{jj'}\sqrt{n_j n_{j'}} (u_{j'\mathbf{k}} - v_{j'\mathbf{k}}) = -\hbar\omega v_{j\mathbf{k}}. \quad (23b)$$

Diagonalizing the eigenvalue equation (23), we obtain the Bogoliubov excitation spectrum.

For simplicity, we assume that  $m_1 = m_2 \equiv m$  and  $g_{11}n_1 = g_{22}n_2 \equiv u$ . Then, the eigenvalue of Eq. (23) has a simple form

$$\hbar\omega = \frac{\hbar}{2} (\mathbf{V}_1 + \mathbf{V}_2) \cdot \mathbf{k} \pm \left[ \varepsilon_0^2 + \varepsilon_r^2 + 2\varepsilon_0 u \pm 2(\varepsilon_0^2 \varepsilon_r^2 + 2\varepsilon_0 \varepsilon_r^2 u + \varepsilon_0^2 u_{12}^2)^{1/2} \right]^{1/2}, \quad (24)$$

where  $\varepsilon_0 = \hbar^2 k^2/(2m)$ ,  $\varepsilon_r = \hbar\mathbf{k} \cdot (\mathbf{V}_1 - \mathbf{V}_2)/2$ , and  $u_{12} = g_{12}(n_1 n_2)^{1/2}$ . The expression in the square brackets in Eq. (24) for the negative sign becomes negative for

$$\max[k_r^2 \cos^2 \chi - 4m(u + u_{12})/\hbar^2, 0] < k^2 < \max[k_r^2 \cos^2 \chi - 4m(u - u_{12})/\hbar^2, 0], \quad (25)$$

where the function max yields the maximum value of the arguments,  $\chi$  is the angle between  $\mathbf{V}_1 - \mathbf{V}_2$  and  $\mathbf{k}$ , and  $k_r = m|\mathbf{V}_1 - \mathbf{V}_2|/\hbar$ . From Eq. (25), the system is dynamically stable when  $k_r^2 < 4m(u - u_{12})/\hbar^2$ . Minimizing the expression in the square bracket of Eq. (24) with respect to  $k$  and  $\chi$ , we find  $\cos^2 \chi = 1$ ; thus, the most unstable wave vector is parallel to the relative velocity.

### C. Crossover between Kelvin–Helmholtz and counter-superflow instabilities

In Sec. IIB, we showed that a CSI emerges when the two components overlap with a relative velocity. We expect that a similar situation arises when the interface between the two components is sufficiently thick in the system discussed in Sec. IIA, since in the interface region the two components overlap considerably and have a relative velocity. In this subsection, we show that a CSI emerges when the interface thickness is much larger than the characteristic wavelength. We also show that similar behavior is observed in miscible condensates separated by a potential gradient.

We consider three types of interfaces: thin and thick interfaces produced by the intercomponent repulsion and an interface produced by a potential gradient; these interfaces are shown in the top panels of Figs. 1 (a), 1 (c), and 1 (d), respectively. The interface thickness produced

by the intercomponent repulsion is characterized by

$$\Delta = \frac{g_{12}}{g} - 1, \quad (26)$$

where  $g \equiv g_{11} = g_{22}$ . For  $\Delta \ll 1$ , the density distribution is approximated as [12]

$$n_j(y) = \frac{n_0}{2} \left[ 1 - (-1)^j \tanh \frac{\sqrt{2\Delta} y}{\xi} \right], \quad (27)$$

where  $\xi = \hbar/(mgn_0)^{1/2}$  is the healing length. The interface thickness is therefore  $\simeq \xi\Delta^{-1/2}$ . The potential gradient in Fig. 1 (d) has the form  $U_1 = -U_2 = Gy$  with  $G > 0$  being a constant, which stabilizes the interface at  $y = 0$ .

To observe KHIs and CSIs in a phase-separated BEC, we perform Bogoliubov analysis. Substituting the stationary state (8) and a small excitation of the form,

$$\phi_j = u_{jk_x}(y) e^{ik_x x - i\omega t} - v_{jk_x}^*(y) e^{-ik_x x + i\omega t}, \quad (28)$$

into the GP equation and taking the first order of  $\phi_j$ , we obtain the Bogoliubov-de Gennes (BdG) equation similar to Eq. (23), in which  $\mathbf{K}_j$  has only the  $x$  component and  $n_j$ ,  $u_{j\mathbf{k}}$ , and  $v_{j\mathbf{k}}$  are replaced by  $n_j(y)$ ,  $u_{jk_x}(y)$ , and  $v_{jk_x}(y)$ , respectively. The BdG equation is diagonalized numerically.

The middle panels in Fig. 1 show the maximum value of the imaginary part of the Bogoliubov frequency  $\text{Im } \omega$

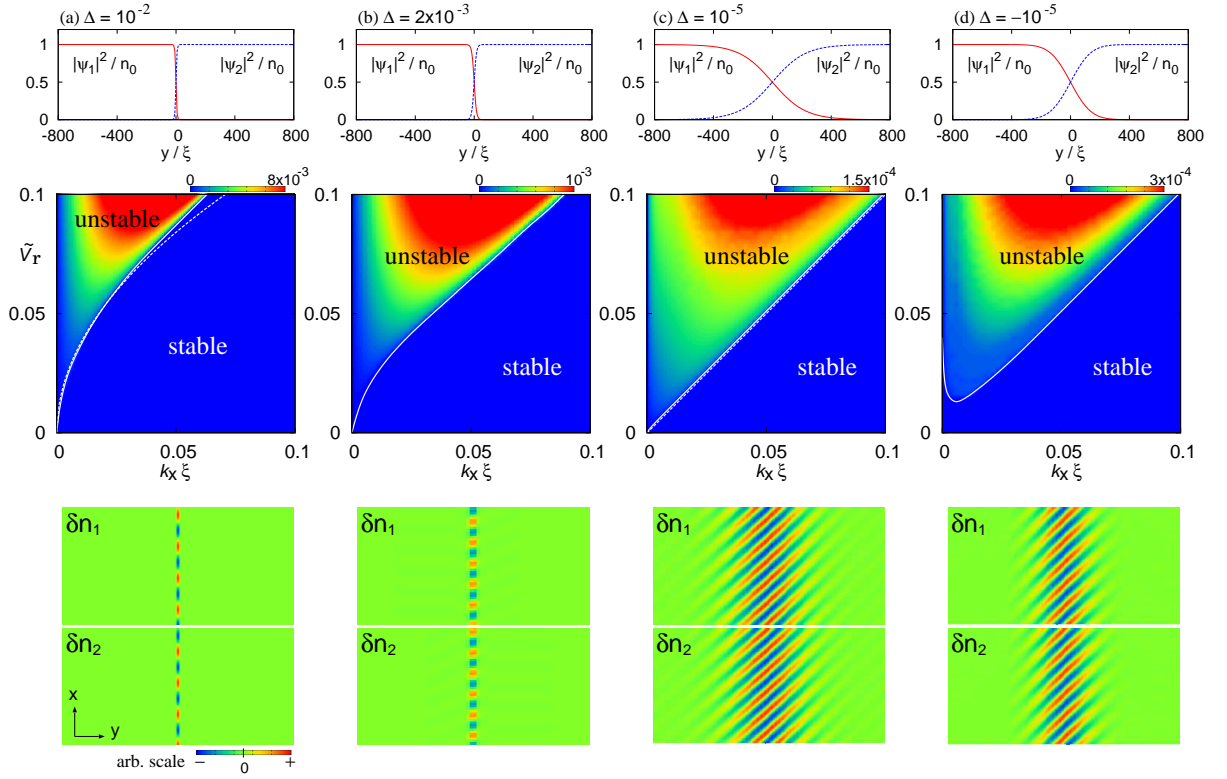


FIG. 1: (Color online) Density distributions of the ground states (top panels), maximum values of the imaginary part in the Bogoliubov spectra (middle panels), and profiles  $\delta n_1(x, y)$  and  $\delta n_2(x, y)$  of the most unstable modes defined in Eq. (34) (bottom panels). The field gradient  $G$  is 0 in (a)–(c) and  $\tilde{G} = m\xi^3 G/\hbar^2 = 10^{-7}$  in (d). In the middle panels, the solid lines indicate the boundaries between dynamically stable and unstable regions and the dashed lines are plots of Eq. (29) in (a) and Eq. (31) in (c). The color bars are normalized by  $gn_0$ . In the bottom panels, the relative velocity is  $\tilde{V}_r = m\xi V_r/\hbar = 0.08$  and the field of view is  $1600\xi \times 800\xi$ . All the results are independent of  $V_1 + V_2$ .

for each relative velocity  $V_r = V_1 - V_2$  and wave number  $k_x$  of the excitation, where the solid lines divide the dynamically stable and unstable regions. The stability boundary for the KHI in Eq. (17) with  $\rho_1 = \rho_2 = mn_0$  has the form

$$k_x = \frac{mn_0 V_r^2}{2\alpha}. \quad (29)$$

The dashed line in the middle panel of Fig. 1 (a) plots Eq. (29) with the interface tension coefficient in Refs. [12, 13] as

$$\alpha = \frac{\hbar n_0^{3/2}}{\sqrt{2m}} \sqrt{g_{12} - g}. \quad (30)$$

The solid and dashed lines agree well for a low relative velocity. If  $G > 0$ , the stability boundary deviates from Eq. (29) for  $k \rightarrow 0$  [6]. The dashed line in the middle panel of Fig. 1 (c) plots

$$k_x = \frac{m}{\hbar} V_r, \quad (31)$$

which is the stability boundary for the CSI in Eq. (25) with  $u = u_{12}$  and  $\chi = 0$ . The dashed line almost overlaps

with the solid line. These facts indicate that the KHI is the dominant instability for the parameters in Fig. 1 (a), whereas the CSI dominates in Fig. 1 (c).

The dominant instability changes from the KHI to the CSI when the interface thickness or the relative velocity increases. The crossover between the two instabilities can be estimated by equating Eqs. (29) and (31),

$$\frac{mn_0 V_r^2}{2\alpha} \sim \frac{m}{\hbar} V_r, \quad (32)$$

which can be rewritten as

$$\frac{\hbar}{m V_r} \sim \frac{\xi}{\sqrt{\Delta}} \quad (33)$$

using Eq. (30). For example, for  $\Delta = 2 \times 10^{-3}$ , the crossover velocity is  $\tilde{V}_r = m\xi V_r/\hbar \sim 0.04$ . This is consistent with the middle panel of Fig. 1 (b), in which the stability boundary is parabolic for  $\tilde{V}_r \ll 0.04$  and linear for  $\tilde{V}_r \gg 0.04$ . Equation (33) indicates that the KHI is the dominant instability when the interface thickness  $\sim \xi \Delta^{-1/2}$  is much smaller than the characteristic wavelength  $\hbar/(m V_r)$  associated with the relative velocity. The CSI is dominant in the opposite limit, i.e.,

$\xi\Delta^{-1/2} \gg \hbar/(mV_r)$ . It should be noted that the stability boundaries in the middle panels of Figs. 1 (a)-1 (c) have the universal form scaled by  $\Delta^{1/2}$ . This is because the healing length  $\xi$  is not relevant in the present problem, and the characteristic length scale for  $G = 0$  is only the interface thickness  $\xi\Delta^{-1/2}$ . In fact, plotting the boundaries with respect to  $k_x\xi\Delta^{1/2}$  and  $\tilde{V}_r\Delta^{1/2}$ , we find that they agree very well.

Another difference between the KHI and the CSI is found in the excitation modes. The bottom panels in Fig. 1 show the change in the density by excitation of the most unstable mode,

$$\delta n_j(x, y) = \left| \sqrt{n_j(y)} + cu_{jk_x}(y)e^{ik_x x} - cv_{jk_x}^*(y)e^{-ik_x x} \right|^2 - n_j(y), \quad (34)$$

where  $c \ll 1$  is a small constant. The first term on the right-hand side of Eq. (34) is the density distribution with a small excitation of the mode. We see that the excitation modes are localized near the interface. In the bottom panel of Fig. 1 (a), the wavelength of the mode is larger than the interface thickness, and the excitation of the mode shifts the interface sinusously. On the other hand, in the bottom panel of Fig. 1 (c), the wavelength of the mode is smaller than the interface thickness, and the dynamical instability develops stripes in the interface region. Interestingly, the stripes are inclined with respect to the interface, whereas the most unstable wave vector is parallel to the relative velocity in the uniform system discussed in Sec. II B.

Figure 1 (d) shows the case of the interface produced by the field gradient  $G > 0$ , where the miscible condition  $\Delta < 0$  is satisfied. The stability boundary in the middle panel of Fig. 1 (d) is similar to that for the immiscible case with the field gradient (Fig. 2 of Ref. [6]). The excitation profile in the bottom panel of Fig. 1 (d) is inclined stripes, just as in Fig. 1 (c). If we apply the same field gradient to the system of Fig. 1 (c), we obtain results similar to Fig. 1 (d) (data not shown).

Figure 2 demonstrates the time evolution of the immiscible system for  $\Delta = 10^{-2}$  and  $10^{-5}$  with no field gradient  $G = 0$  and the miscible system for  $\Delta = -10^{-5}$  with a field gradient  $G > 0$ , where the relative velocity is  $\tilde{V}_r = 0.1$  with  $V_1 + V_2 = 0$ . The initial state is the stationary state of the GP equation with small white noise to break the translation symmetry and trigger the dynamical instability. The time evolution is obtained by solving the GP equation by the pseudospectral method. For  $\Delta = 10^{-2}$  [Fig. 2 (a)], the KHI is dominant, corresponding to Fig. 1 (a). We see that the interface is modulated due to the KHI ( $\tilde{t} = gn_0 t/\hbar = 5000$ ). In Figs. 2 (b) and 2 (c), the interface is much thicker and the CSI is dominant; modulation arises in the region where the two components overlap. The nonlinear dynamics and vortex creation are quite different in the cases of the KHI and the CSI. In the former, quantized vortices are formed at the peaks and troughs of the wave, and enter into each component from the interface [6]. In contrast, in the latter,

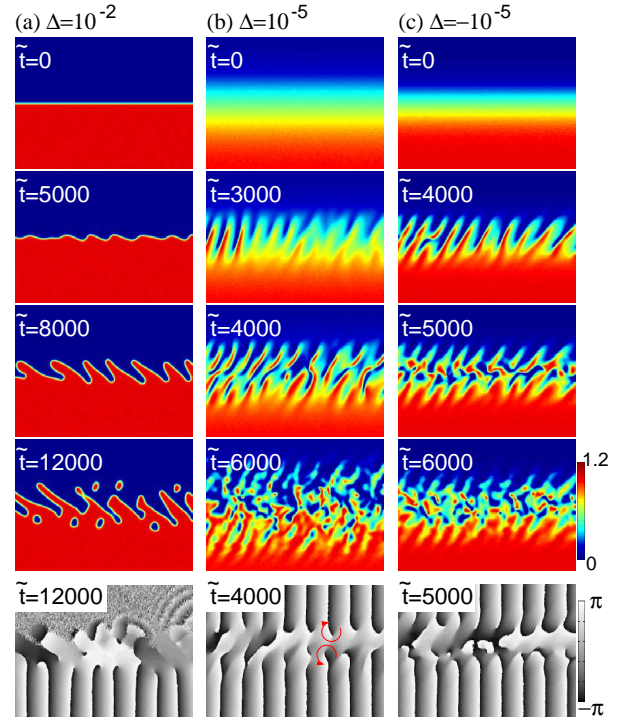


FIG. 2: (Color online) Time evolution of the two-component BEC for (a)  $\Delta = 10^{-2}$  with  $\tilde{G} = 0$ , (b)  $\Delta = 10^{-5}$  with  $\tilde{G} = 0$ , and (c)  $\Delta = -10^{-5}$  with  $\tilde{G} = 10^{-7}$ . The relative velocity is  $\tilde{V}_r = 0.1$  with  $V_1 + V_2 = 0$ . The four upper rows are the density profiles  $|\psi_1|^2$  and the bottom panels are the phase profiles  $\arg \psi_1$ . The arrows in the bottom panel indicate an example of a vortex pair. The density is normalized by  $gn_0$ . Time  $t$  is normalized as  $\tilde{t} = gn_0 t/\hbar$ . The field of view is  $1000\xi \times 750\xi$ .

vortex pairs are created in the interface region (arrows in the bottom panels), which are subsequently disturbed in a complicated manner. In all the cases in Fig. 2, the total density  $|\psi_1|^2 + |\psi_2|^2$  is almost constant throughout the dynamics.

### III. INSTABILITIES IN PANCAKE-SHAPED SYSTEMS

#### A. Kelvin-Helmholtz instability

We have considered an ideal flat interface in Sec. II. In the following sections, we propose realistic systems for experimental observation of interfacial instabilities in trapped BECs.

We first consider an axisymmetric harmonic potential given by

$$U_1(\mathbf{r}) = U_2(\mathbf{r}) = \frac{1}{2}m[\omega_\perp^2(x^2 + y^2) + \omega_z^2 z^2], \quad (35)$$

where the radial and axial trap frequencies are  $\omega_\perp = 2\pi \times 80$  Hz and  $\omega_z = 2\pi \times 4$  kHz, respectively. Since  $\hbar\omega_z$  is much larger than other characteristic energies,



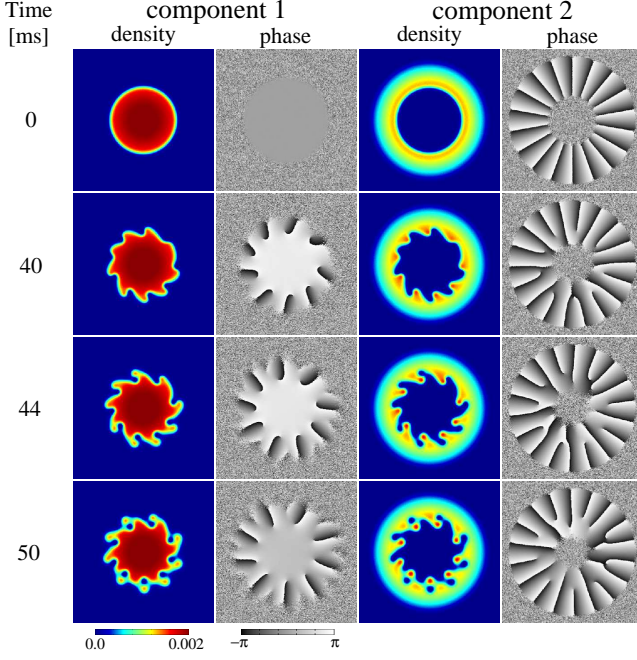


FIG. 3: (Color online) Time evolution of the density and phase profiles. In the initial state, component 2 rotates with vorticity  $n_2 = 18$  and component 1 is at rest. The total number of  $^{23}\text{Na}$  atoms is  $N = 1.63 \times 10^6$  with an equal population in each component. The field of view is  $93 \times 93 \mu\text{m}$ . The unit of density is  $N/a_\perp^2$  with  $a_\perp = [\hbar/(m\omega_\perp)]^{1/2}$ .

we reduce the system to two dimensions (2D) in the simulation. Assuming that the wave function can be written as  $\psi(\mathbf{r}) = \psi_\perp(x, y)\psi_z(z)$  with  $\psi_z(z)$  being the ground state of the harmonic oscillator, and integrating the GP equation with respect to  $z$ , we obtain the 2D GP equation with the effective interaction coefficient  $g_{jj'}^{2D} = [m\omega_z/(2\pi\hbar)]^{1/2}g_{jj'}$ . Components 1 and 2 are assumed to be respectively the hyperfine states  $|F, m_F\rangle = |1, 0\rangle$  and  $|1, 1\rangle$  of  $^{23}\text{Na}$  atoms. The scattering lengths measured in Refs. [17, 18] give  $a_{11} \simeq 53.4a_B$  and  $a_{12} = a_{22} \simeq 54.2a_B$  with  $a_B$  being the Bohr radius, which satisfy the condition of phase separation (4). A strong magnetic field suppresses the spin exchange dynamics,  $|0, 0\rangle|0, 0\rangle \rightarrow |1, 1\rangle|1, -1\rangle$ , due to the quadratic Zeeman effect [19].

The initial state is prepared as follows. We first calculate the ground state  $|\psi_j\rangle$  with a centrifugal potential  $\hbar^2 n_j^2 / [2m(x^2 + y^2)]$  by the imaginary-time propagation of the GP equation. We then give the phases as

$$\psi_j = e^{in_j\theta} |\psi_j| \quad (j = 1, 2), \quad (36)$$

where the integer  $n_j$  is the vorticity of the  $j$ th component and  $\theta = \arg(x + iy)$ . This procedure is efficient for preparing an axisymmetric rotating stationary state. We thus obtain a stationary state with shear flow at the interface, as shown in the top panels in Fig. 3, where  $n_1 = 0$  and  $n_2 = 18$ . Because  $a_{22} > a_{11}$  and the centrifugal force on component 2, component 1 occupies the

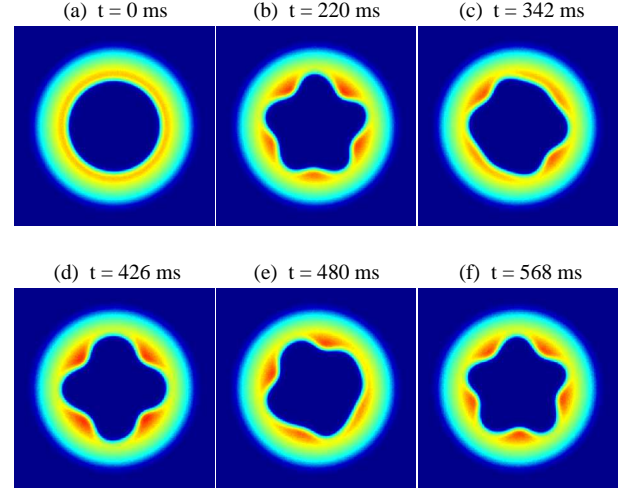


FIG. 4: (Color online) Time evolution of the density profile of component 2 for  $n_2 = 12$ . Other parameters are the same as those in Fig. 3.

center and component 2 surrounds it. The presence of component 1 stabilizes the vortices in component 2. We add small numerical noise to the initial state to break the axisymmetry. The two components are assumed to have the same number of atoms in the following analysis.

Figure 3 shows the subsequent time evolution. At  $t = 40$  ms, a wavy pattern develops at the interface due to the KHI [6], which has approximately nine-fold symmetry. The wave at the interface then grows ( $t = 44$  ms) and quantized vortices are released from the peaks and the troughs of the wave into both components ( $t = 50$  ms). This interface behavior is similar to that in the flat interface [Fig. 2 (a)]. When the relative velocity at the interface is below a critical velocity ( $n_2 < 12$ ), symmetry-breaking dynamics does not occur, whereas the flat interface is always unstable for a nonzero relative velocity [see Eq. (17)]. This indicates that in the trapped system the effective force is exerted on the interface [see Eq. (14)], which originates from the trap potential and the centrifugal force.

Figure 4 shows the time evolution of component 2 for a relative velocity just above the critical value ( $n_2 = 12$ ). A five-fold pattern first emerges [Fig. 4 (b)], which changes to a four-fold pattern [Fig. 4 (d)] and then returns to a five-fold pattern [Fig. 4 (f)]. In contrast to the case of  $n_2 = 18$  shown in Fig. 3, the deformation of the interface is moderate and no quantized vortices are generated throughout the dynamics. Estimating the unstable wavelengths in Figs. 3 and 4 from the analytic expression (16) is difficult because of an ambiguity in the interface tension coefficient  $\alpha$  in inhomogeneous systems with a curved interface.

## B. Bogoliubov analysis

We perform Bogoliubov analysis of a quasi-2D trapped system. We write the wave function as

$$\psi_j(r, \theta) = [f_j(r) + \phi_j(r, \theta)] e^{in_j\theta} e^{-i\mu_j t/\hbar}, \quad (37)$$

where  $f_j(r)e^{in_j\theta}$  is the stationary state,  $\phi_j$  is a small excitation,  $\mu_j$  is the chemical potential, and  $r = (x^2 +$

$y^2)^{1/2}$ . We expand the small excitation  $\phi_j$  as

$$\phi_j(r, \theta) = u_{jL}(r)e^{iL\theta - i\omega t} - v_{jL}^*(r)e^{-iL\theta + i\omega t}, \quad (38)$$

where  $L$  is an integer and the excitation has  $L$ -fold symmetry. Substituting Eqs.(37) and (38) into the GP equation and taking the first order of  $\phi_j$ , we obtain the BdG equation ( $j \neq j'$ ),

$$\left\{ -\frac{\hbar^2}{2m} \left[ \frac{\partial^2}{\partial r^2} + \frac{1}{r} \frac{\partial}{\partial r} - \frac{(n_j + L)^2}{r^2} \right] + U_j - \mu_j + 2g_{jj}^{2D} f_j^2 + g_{jj'}^{2D} f_{j'}^2 \right\} u_{jL} - g_{jj}^{2D} f_j^2 v_{jL} + g_{jj'}^{2D} f_j f_{j'} (u_{j'L} - v_{j'L}) = \hbar\omega u_{jL}, \quad (39a)$$

$$\left\{ -\frac{\hbar^2}{2m} \left[ \frac{\partial^2}{\partial r^2} + \frac{1}{r} \frac{\partial}{\partial r} - \frac{(n_j - L)^2}{r^2} \right] + U_j - \mu_j + 2g_{jj}^{2D} f_j^2 + g_{jj'}^{2D} f_{j'}^2 \right\} v_{jL} - g_{jj}^{2D} f_j^2 u_{jL} - g_{jj'}^{2D} f_j f_{j'} (u_{j'L} - v_{j'L}) = -\hbar\omega v_{jL}. \quad (39b)$$

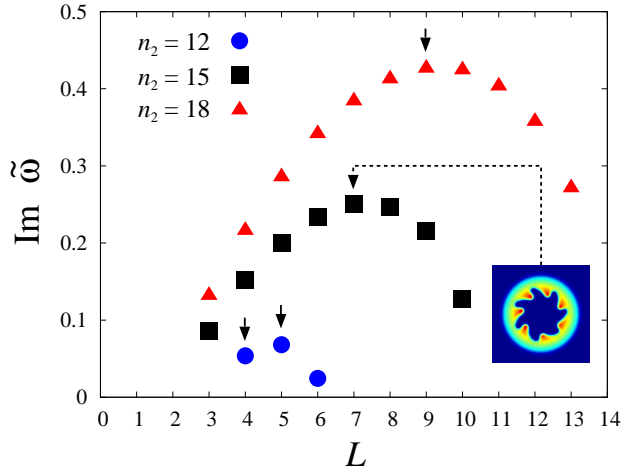


FIG. 5: (Color online) Imaginary part of Bogoliubov frequency  $\tilde{\omega} = \omega/\omega_{\perp}$  for  $n_1 = 0$  and  $n_2 = 12$  (circles),  $n_2 = 15$  (squares), and  $n_2 = 18$  (triangles). The excitation mode has  $L$ -fold symmetry. The total number of atoms is  $N = 1.63 \times 10^6$ . The conditions for triangles and circles are the same as those in Figs. 3 and 4, respectively. The solid arrows indicate the modes relevant to the patterns in Figs. 3 and 4. The inset shows a snapshot of the density profile of component 2 obtained by time evolution for  $n_2 = 15$ .

We numerically diagonalize Eq. (39).

Figure 5 shows the imaginary part of the excitation frequency for the same conditions as those in Fig. 3 ( $n_2 = 18$ , triangles) and Fig. 4 ( $n_2 = 12$ , circles). For  $n_2 = 18$ , the imaginary part is a maximum for  $L = 9$ , which is consistent with the nine-fold pattern in Fig. 3. The emergence of the four and five-fold patterns in Fig. 4 is understood from the fact that the corresponding imag-

inary parts are close to each other (the circles indicated by the arrows in Fig. 5). In fact, we numerically confirmed that for  $n_2 = 18$ , a nine-fold pattern or a 10-fold pattern emerges depending on the initial random noise. For  $n_2 < 12$ , no imaginary part appears. For the condition in Fig. 5, only the lowest mode becomes dynamically unstable for each  $L$ .

## C. Counter-superflow instability

We next consider the CSI in the pancake-shaped system. We use the hyperfine states  $|1, 1\rangle$  and  $|1, 0\rangle$  of  $^{87}\text{Rb}$  atoms for components 1 and 2. According to Ref. [20], the scattering lengths are  $a_{11} = a_{12} = 100.4a_B$  and  $a_{22} = 100.9a_B$ , which satisfy the miscible condition (19). We employ the harmonic potential plus a central optical plug given by

$$U_1(\mathbf{r}) = U_2(\mathbf{r}) = \frac{1}{2}m[\omega_{\perp}^2(x^2 + y^2) + \omega_z^2 z^2] + \hbar\omega_{\perp}\alpha e^{-\beta(x^2 + y^2)/a_{\perp}^2}, \quad (40)$$

where  $\alpha$  and  $\beta$  are dimensionless parameters respectively characterizing the strength and the width of the optical plug, and  $a_{\perp} = [\hbar/(m\omega_{\perp})]^{1/2}$ . The same trap frequencies as those in Sec. III A are used and hence the calculation is performed in 2D. We choose the parameters of the optical plug to be  $\alpha = 1000$  and  $\beta = 0.01$ . The optical plug is necessary for  $n_1 \neq 0$  and  $n_2 \neq 0$  to eliminate undesirable instability. If the optical plug is absent, one component flows into the vortex core of the other component and the axisymmetry is broken before the CSI emerges.

Figure 6 shows the time evolution of counterrotating condensates with initial vorticities  $n_1 = -20$  and  $n_2 = 30$ . Despite the miscible condition, the two condensates

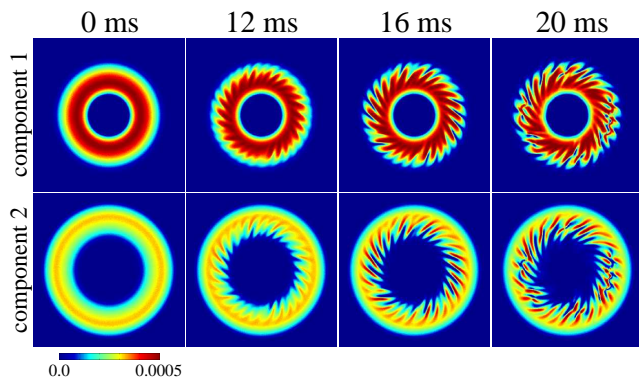


FIG. 6: (Color online) Time evolution of the density profiles for counter-rotating miscible condensates. The vorticities of the initial state are  $n_1 = -20$  and  $n_2 = 30$ . The total number of  $^{87}\text{Rb}$  atoms is  $N = 3.19 \times 10^6$  with an equal population in each component. The field of view is  $84 \times 84 \mu\text{m}$ .

are weakly separated ( $t = 0$  ms of Fig. 6) because of the difference in the centrifugal force. As time develops, a saw-toothed pattern emerges at the interface, as shown in Fig. 6. This behavior at the interface is similar to that in Figs. 2 (b) and 2 (c), indicating that the symmetry-breaking dynamics is driven by the CSI. The relation between the CSI and quantum turbulence has recently been studied [21].

#### IV. INSTABILITIES IN CIGAR-SHAPED SYSTEMS

##### A. Kelvin–Helmholtz instability

We propose two systems for observing the KHI in a cigar-shaped geometry.

The first one is similar to that in Sec. III A; non-rotating component 1 is surrounded by rotating component 2. We use a harmonic potential in Eq. (35) with  $\omega_\perp = 2\pi \times 40$  Hz and  $\omega_z = 2\pi \times 8$  Hz. Components 1 and 2 are respectively the hyperfine states  $|2, 1\rangle$  and  $|1, -1\rangle$  of  $^{87}\text{Rb}$  [22]. The ratio between the scattering lengths of these states is  $a_{11} : a_{12} : a_{22} = 0.97 : 1.0 : 1.03$  with their average being 5.5 nm [23, 24], which satisfy the immiscible condition (4).

We solve the GP equation by performing a 3D numerical simulation. Figure 7 (a) shows the time evolution of the cross-section densities  $|\psi_1(x, y, 0)|^2$  and  $|\psi_2(x, y, 0)|^2$  for the initial vorticities  $n_1 = 0$  and  $n_2 = 7$ . The initial state has an axisymmetric interface with a relative velocity. At  $t = 72$  ms, a wavy pattern with four-fold symmetry develops at the interface due to the KHI. Vortex lines are then released from the interface into both components at  $t = 84$  ms as shown in Figs. 7 (a) and 7 (b). For a smaller relative velocity at the interface (e.g.,  $n_1 = 0$  and  $n_2 = 1$ ), symmetry breaking dynamics does not occur, indicating the existence of a critical velocity,

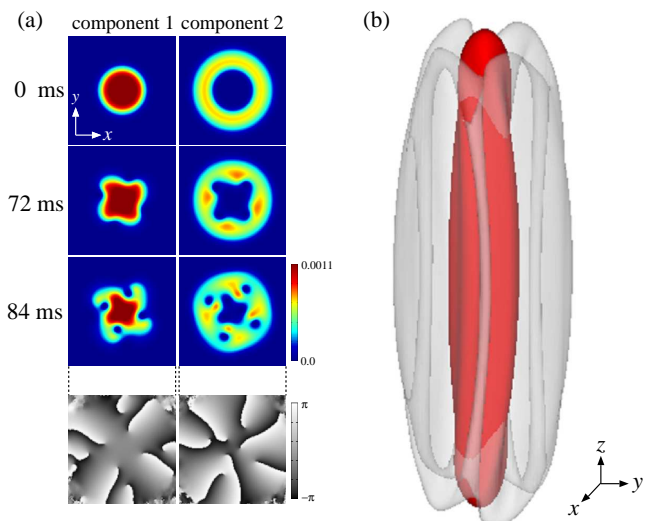


FIG. 7: (Color online) (a) Time evolution of the cross-section densities  $|\psi_1(x, y, 0)|^2$  (left panels) and  $|\psi_2(x, y, 0)|^2$  (right panels) for  $n_1 = 0$  and  $n_2 = 7$ . The field of view is  $20 \times 20 \mu\text{m}$ . The total number of  $^{87}\text{Rb}$  atoms is  $N = 1.75 \times 10^5$  with an equal population in each component. The bottom panels show the phase profiles at  $t = 84$  ms. (b) Isodensity surfaces of component 1 (inside) and component 2 (outside) at  $t = 84$  ms. For clarity, only the surface of component 2 is transparent.

as in the case of Sec. III A.

The second configuration for observing the KHI in a cigar-shaped trap is shown in Fig. 8 (a), where components 1 and 2 are located in the  $z \lesssim 0$  and  $z \gtrsim 0$  regions and their interface lies on  $z \simeq 0$ . We use the same hyperfine states of  $^{23}\text{Na}$  as those used in Sec. III A. The potential in Eq. (40) is used with  $\omega_\perp = 2\pi \times 40$  Hz,  $\omega_z = 2\pi \times 8$  Hz,  $\alpha = 50$ , and  $\beta = 0.4$ . The optical plug is applied to prevent one component flowing into the vortex core of the other component. We apply a magnetic field gradient of  $dB/dz = -17.3$  mG/cm, which pushes component 2 ( $|1, 1\rangle$ ) in the  $+z$  direction. This force controls the strength of the KHI.

Figure 8 (b) depicts the time evolution of the system with initial vorticities of  $n_1 = 2$  and  $n_2 = -2$ . The relative velocity at the interface induces the KHI, which breaks the axisymmetry and deforms the interface [280 ms of Fig. 8 (b)]. A quantized vortex is then released from the interface into each component at  $t \simeq 298$  ms. The vortex lines lie in the radial direction; in contrast, the vortex lines lie along the  $z$  direction in Fig. 7.

##### B. Counter-superflow instability

As shown in Sec. II, the interfacial instability is dominated by the CSI when the overlap between the two components is large. We study this situation for a cigar-shaped system. The two components are the same hyperfine states of  $^{87}\text{Rb}$  as those used in Sec. III C, and the



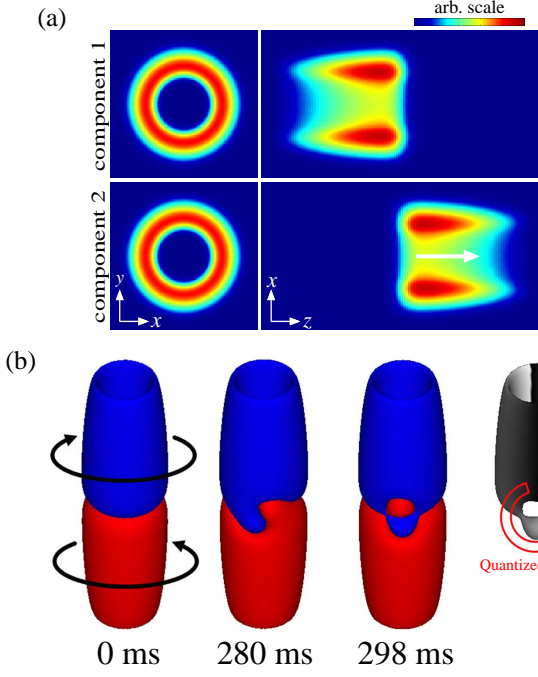


FIG. 8: (Color online) (a) Column densities  $\int dz |\psi_j|^2$  (left panels,  $40 \times 40 \mu\text{m}$ ) and  $\int dy |\psi_j|^2$  (right panels,  $40 \times 132 \mu\text{m}$ ) of the initial state for  $n_1 = 2$  and  $n_2 = -2$ . The white arrow indicates the direction of the Stern-Gerlach force produced by the field gradient of  $dB/dz = -17.3 \text{ mG/cm}$ . (b) Time evolution of the isodensity surfaces of components 1 (lower) and 2 (upper). The solid arrows at  $t = 0$  ms indicate the directions of the rotation. The phase profile of component 2 at  $t = 298$  ms is shown in the rightmost image. The total number of  $^{23}\text{Na}$  atoms is  $N = 6.6 \times 10^5$  with an equal population in each component.

potential is the same as that in Sec. IV A.

Figure 9 shows the time evolution of the system for initial vorticities of  $n_1 = 3$  and  $n_2 = -3$ . Since the scattering lengths satisfy the miscible condition and the field gradient is small, the two components in the initial stationary state widely overlap with each other [Fig. 9 (a)]. The time evolution in Fig. 9 (b) is similar to those in Figs. 2 (b) and 2 (c) in the sense that stripes of the two components are formed where they overlap. The spiral pattern in Fig. 9 (b) ( $t \simeq 40$  ms) corresponds to the inclination of the stripes in Figs. 1 (d) and 2 (c).

## V. CONCLUSIONS

We have studied the dynamical instabilities at an interface of a two-component BEC with a relative velocity between the two components. When the two components are strongly segregated and the interface thickness is negligible, a KHI is generated at the interface. On the other hand, when the interface thickness is much larger than the unstable wavelength, a CSI dominates over the KHI. We have proposed realistic experimental systems

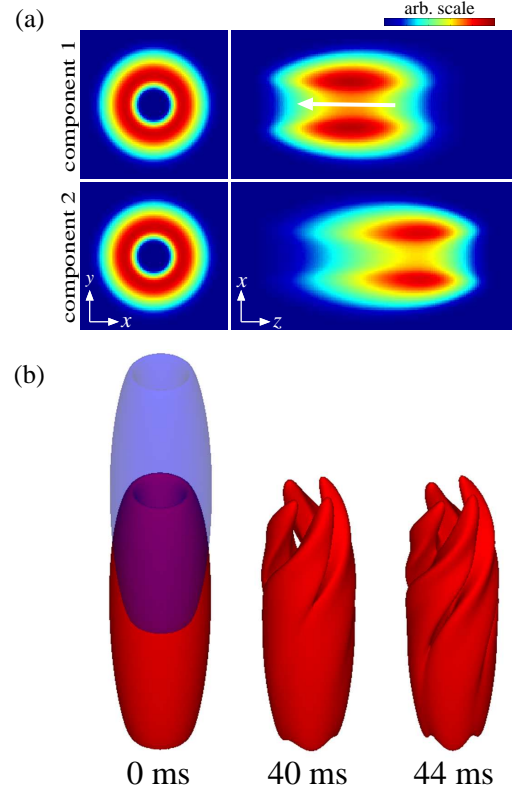


FIG. 9: (Color online) (a) Column densities  $\int dz |\psi_j|^2$  (left panels,  $27 \times 27 \mu\text{m}$ ) and  $\int dy |\psi_j|^2$  (right panels,  $27 \times 118 \mu\text{m}$ ) of the initial state for  $n_1 = 3$  and  $n_2 = -3$ . The white arrow shows the direction of the Stern-Gerlach force produced by a field gradient of  $dB/dz = 0.34 \text{ mG/cm}$ . (b) Time evolution of the isodensity surface of component 1. At  $t = 0$ , component 2 is also shown as the transparent surface. The total number of  $^{87}\text{Rb}$  atoms is  $N = 1.3 \times 10^6$  with an equal population in each component.

of  $^{23}\text{Na}$  and  $^{87}\text{Rb}$  BECs in pancake-shaped and cigar-shaped traps. In a pancake-shaped trap, a KHI can be observed at the interface of two components separated inside and outside, and rotating with different vorticities (Figs. 3 and 4). The patterns produced by the KHI are consistent with the Bogoliubov analysis (Fig. 5). Using miscible two components, a CSI can also be realized (Fig. 6). For a cigar-shaped trap, we proposed two configurations for observing the KHI: the two components separate radially (Fig. 7) or in the  $z$  direction (Fig. 8). The vortex lines released from the interface lie along the radial direction in the former, whereas they lie along the  $z$  direction in the latter. The interface thickness can be controlled using the miscible condensates with a magnetic field gradient in the  $z$  direction (Fig. 9).

The initial states used in Secs. III and IV are multiply quantized vortices with different vorticities in the two components. Such states can be prepared using Laguerre-Gaussian beams [25] or topological phase imprinting [26]. Multiply quantized vortex states with large vorticities can in principle be generated by repeated ap-

plication of these methods [27, 28].

The dynamics caused by the KHI and the CSI in quantum fluids are quite different from those in classical fluids, since vortices are quantized and there is no viscosity. Moreover, in the present system, the miscibility of the two components can be dynamically controlled by Feshbach resonance [29, 30]. These features of BECs renew our interest in fluid instabilities [16, 31–33] and may provide new physical insights into fluid dynamics.

## Acknowledgments

This work was supported by KAKENHI from JSPS and MEXT (Nos. 199748, 17071005, 17071008, 20540388, 21340104, 21740267, and 22340116).

- 
- [1] H. von Helmholtz, *Phil. Mag.* **36**, 337 (1868).
  - [2] Lord Kelvin, *Phil. Mag.* **42**, 362 (1871).
  - [3] See, for example, H. Lamb, *Hydrodynamics*, 6th ed. (Dover, New York, 1945), Sec. 232; L. D. Landau and E. M. Lifshitz, *Fluid Mechanics*, 2nd ed. (Butterworth-Heinemann, Oxford, 1987), Sec. 62.
  - [4] R. Blaauwgeers, V. B. Eltsov, G. Eska, A. P. Finne, R. P. Haley, M. Krusius, J. J. Ruohio, L. Skrbek, and G. E. Volovik, *Phys. Rev. Lett.* **89**, 155301 (2002).
  - [5] G. E. Volovik, *Pis'ma Zh. Eksp. Teor. Fiz.* **75**, 491 (2002) [*JETP Lett.* **75**, 418 (2002)].
  - [6] H. Takeuchi, N. Suzuki, K. Kasamatsu, H. Saito, and M. Tsubota, *Phys. Rev. B* **81**, 094517 (2010).
  - [7] C. K. Law, C. M. Chan, P. T. Leung, and M.-C. Chu, *Phys. Rev. A* **63**, 063612 (2001).
  - [8] M. A. Hoefer, C. Hamner, J. J. Chang, and P. Engels, *arXiv:1007.4947*.
  - [9] H. Takeuchi, N. Suzuki, K. Kasamatsu, H. Saito, and M. Tsubota, *J. Low Temp. Phys.* **158**, 384 (2010).
  - [10] C. J. Pethick and H. Smith, *Bose-Einstein Condensation in Dilute Gases*, 2nd ed. (Cambridge University Press, Cambridge, 2008).
  - [11] P. Ao and S. T. Chui, *Phys. Rev. A* **58**, 4836 (1998).
  - [12] R. A. Barankov, *Phys. Rev. A* **66**, 013612 (2002).
  - [13] B. Van Schaeybroeck, *Phys. Rev. A* **78**, 023624 (2008); **80**, 065601 (2009).
  - [14] Lord Rayleigh, *Proc. London Math. Soc.* **14**, 170 (1883).
  - [15] G. I. Taylor, *Proc. Roy. Soc. London Ser. A* **201**, 192 (1950).
  - [16] K. Sasaki, N. Suzuki, D. Akamatsu, and H. Saito, *Phys. Rev. A* **80**, 063611 (2009).
  - [17] A. Crubellier, O. Dulieu, F. Masnou-Seeuws, M. Elbs, H. Knöckel, and E. Tiemann, *Eur. Phys. J. D* **6**, 211 (1999).
  - [18] A. T. Black, E. Gomez, L. D. Turner, S. Jung, and P. D. Lett, *Phys. Rev. Lett.* **99**, 070403 (2007).
  - [19] H. -J. Miesner, D. M. Stamper-Kurn, J. Stenger, S. Inouye, A. P. Chikkatur, and W. Ketterle, *Phys. Rev. Lett.* **82**, 2228 (1999).
  - [20] E. G. M. van Kempen, S. J. J. M. F. Kokkelmans, D. J. Heinzen, and B. J. Verhaar, *Phys. Rev. Lett.* **88**, 093201 (2002).
  - [21] S. Ishino, H. Takeuchi, and M. Tsubota, *arXiv:1006.4488*; H. Takeuchi, S. Ishino, and M. Tsubota, *arXiv:1008.4664*.
  - [22] For the hyperfine states used in Sec. III A, the phase separation occurs in the  $z$  direction.
  - [23] M. R. Matthews, D. S. Hall, D. S. Jin, J. R. Ensher, C. E. Wieman, E. A. Cornell, F. Dalfovo, C. Minniti, and S. Stringari, *Phys. Rev. Lett.* **81**, 243 (1998).
  - [24] D. S. Hall, M. R. Matthews, J. R. Ensher, C. E. Wieman, and E. A. Cornell, *Phys. Rev. Lett.* **81**, 1539 (1998).
  - [25] M. F. Andersen, C. Ryu, P. Cladé, V. Natarajan, A. Vaziri, K. Helmerson, and W. D. Phillips, *Phys. Rev. Lett.* **97**, 170406 (2006).
  - [26] A. E. Leanhardt, A. Görlitz, A. P. Chikkatur, D. Kielpinski, Y. Shin, D. E. Pritchard, and W. Ketterle, *Phys. Rev. Lett.* **89**, 190403 (2002).
  - [27] M. Möttönen, V. Pietilä, and S. M. M. Virtanen, *Phys. Rev. Lett.* **99**, 250406 (2007).
  - [28] Z. F. Xu, P. Zhang, C. Raman, and L. You, *Phys. Rev. A* **78**, 043606 (2008); Z. F. Xu, P. Zhang, R. Lü, and L. You, *Phys. Rev. A* **81**, 053619 (2010).
  - [29] S. B. Papp, J. M. Pino, and C. E. Wieman, *Phys. Rev. Lett.* **101**, 040402 (2008).
  - [30] S. Tojo, Y. Taguchi, Y. Masuyama, T. Hayashi, H. Saito, and T. Hirano, to be published in *Phys. Rev. A*.
  - [31] S. Gautam and D. Angom, *Phys. Rev. A* **81**, 053616 (2010).
  - [32] K. Sasaki, N. Suzuki, and H. Saito, *Phys. Rev. Lett.* **104**, 150404 (2010).
  - [33] A. Bezett, V. Bychkov, E. Lundh, D. Kobayakov, and M. Marklund, *arXiv:1006.2261*.